**RESEARCH ARTICLE**

ADVANCED ENERGY MATERIALS

www.advenergymat.de

# Nanocomposites: A New Opportunity for Developing Highly Active and Durable Bifunctional Air Electrodes for Reversible Protonic Ceramic Cells

*Yufei Song, Jiapeng Liu, Yuhao Wang, Daqin Guan, Arim Seong, Mingzhuang Liang, Matthew J. Robson, Xiandong Xiong, Zhiqi Zhang, Guntae Kim, Zongping Shao,* and Francesco Ciucci**

**Reversible protonic ceramic cells (RePCCs) can facilitate the global transition to renewable energy sources by providing high efficiency, scalable, and fuel-flexible energy generation and storage at the grid level. However, RePCC technology is limited by the lack of durable air electrode materials with high activity toward the oxygen reduction/evolution reaction and water formation/water-splitting reaction. Herein, a novel nanocomposites concept for developing bifunctional RePCC electrodes with exceptional performance is reported. By harnessing the unique functionalities of nanoscale particles, nanocomposites can produce electrodes that simultaneously optimize reaction activity in both fuel cell/electrolysis operations. In this work, a nanocomposite electrode composed of tetragonal and Ruddlesden–Popper (RP) perovskite phases with a surface enriched by $CeO_2$ and NiO nanoparticles is synthesized. Experiments and calculations identify that the RP phase promotes hydration and proton transfer, while NiO and $CeO_2$ nanoparticles facilitate $O_2$ surface exchange and $O^{2-}$ transfer from the surface to the major perovskite. This composite also ensures fast ($H^+$/$O^{2-}$/$e^-$) triple-conduction, thereby promoting oxygen reduction/evolution reaction activities. The as-fabricated RePCC achieves an excellent peak power density of 531 mW $cm^{-2}$ and an electrolysis current of –364 mA $cm^{-2}$ at 1.3 V at 600 °C, while demonstrating exceptional reversible operation stability of 120 h at 550 °C.**

## 1. Introduction

Rapid global population growth and economic progress through industrialization has caused significant damage to the global climate. Renewable energy sources, such as solar and wind, are projected to be instrumental in achieving a sustainable global power supply while combatting environmental pollution.[1] However, these renewable energy sources are non-dispatchable, and cannot meet instantaneous demand. Consequently, energy storage devices are needed to buffer power production. Solid oxide cells (SOCs) are extremely promising for grid-scale energy conversion and storage, as they can convert the chemical energy from a wide range of fuels into electrical power in fuel cell mode, with far higher thermodynamic efficiencies and lower emissions than conventional combustion-based systems.[2–5] SOCs can also operate reversibly, storing electrical energy through water-splitting and storage of hydrogen gas in electrolysis mode. In addition, fuel cell storage capacity is independent of device size, and limited only by fuel storage tank volume, posing a significant advantage over rechargeable batteries.[6–9]

SOCs can be either oxygen- (O-SOC) or proton- (H-SOC) conducting, depending on electrolyte composition.[2,5,10,11] In particular, solid oxide electrolysis cells based on proton-conducting electrolytes (PCECs) have three unique advantages over conventional (oxygen ion-conducting) solid oxide electrolysis cells (O-SOECs). First, the

Y. Song, J. Liu, Y. Wang, M. J. Robson, Z. Zhang, F. Ciucci
Department of Mechanical and Aerospace Engineering
The Hong Kong University of Science and Technology
Clear Water Bay, Hong Kong, China
E-mail: francesco.ciucci@ust.hk

D. Guan, M. Liang, X. Xiong, Z. Shao
State Key Laboratory of Materials-Oriented Chemical Engineering
College of Chemical Engineering
Nanjing Tech University
Nanjing 210009, China
E-mail: shaozp@njtech.edu.cn

The ORCID identification number(s) for the author(s) of this article can be found under https://doi.org/10.1002/aenm.202101899.

A. Seong, G. Kim
Department of Energy Engineering
School of Energy and Chemical Engineering
Ulsan National Institute of Science and Technology
Ulsan 44919, Republic of Korea

Z. Shao
WA School of Mines: Minerals
Energy and Chemical Engineering (WASM-MECE)
Curtin University
Perth, WA 6845, Australia

F. Ciucci
Department of Chemical and Biological Engineering
The Hong Kong University of Science and Technology
Clear Water Bay, Hong Kong, China

**DOI: 10.1002/aenm.202101899**

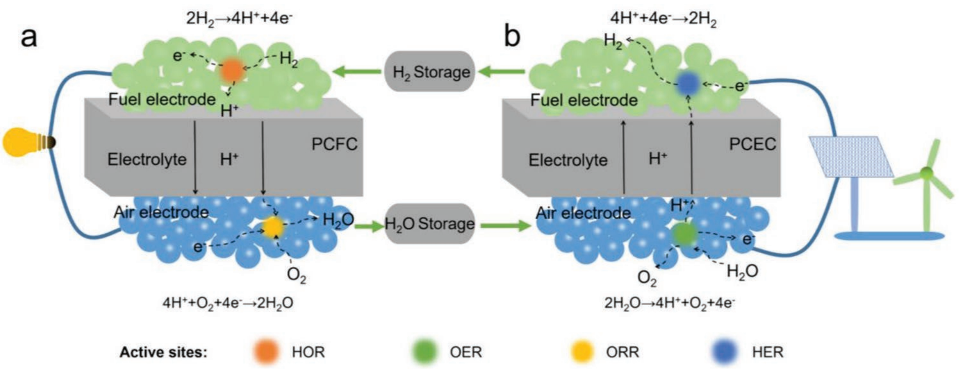

**Figure 1.** Schematic of a reversible protonic ceramic cells (RePCC) operating in a) fuel cell and b) electrolysis mode. HOR, hydrogen oxidation reaction; OER, oxygen evolution reaction; ORR, oxygen reduction reaction; HER, hydrogen evolution reaction.

lower activation energy of proton conduction compared to oxygen conduction results in lower operating temperatures for PCECs than O-SOECs. In turn, decreasing operating temperature improves operational stability and reduces system complexity and costs.[12,13] Second, PCECs produce pure and dry hydrogen that can be compressed and stored directly, thereby removing the need for complex downstream drying, reducing system cost, and complexity.[14] Third, in SOECs, water splitting occurs at the fuel electrode, leading to oxidation/coarsening of the Ni catalysts and increasing the risk of electrode delamination caused by the OER.[15] In contrast, in PCECs, these issues are negated, no water is electrolyzed at the fuel electrode. Recently, it has been proposed that the functionalities of protonic ceramic fuel cells (PCFCs) and PCECs are combined in RePCCs (**Figure 1**).[16–18]

The major challenge that hinders RePCC commercialization is the lack of bifunctional air electrodes (i.e., electrodes with high activity toward both the ORR and OER with suitable long-term stability). In a RePCC, high ORR activity is associated with fast surface exchange ($O_2$ adsorption/dissociation), good $O_2$ diffusion, and $H^+/O^{2-}/e^-$ triple conduction, whereas high OER activity is associated with a fast surface exchange (hydration) and $H^+/e^-$ conduction.[7] Therefore, the bifunctional air electrode for RePCC should possess excellent conduction and exchange properties of $H^+/O^{2-}/e^-$ and stability under RePCC operating conditions. However, single-phase perovskite-based materials have thus far been unable to simultaneously meet all RePCC requirements. For example, although electrocatalytically active mixed ionic and electronic conducting perovskite materials, such as $La_{0.8}Sr_{0.2}CoO_{3-\delta}$,[19] $La_{0.6}Sr_{0.4}Co_{0.2}Fe_{0.8}O_{3-\delta}$, and $Ba_{0.5}Sr_{0.5}Co_{0.8}Fe_{0.2}O_{3-\delta}$,[20–22] can be candidates for RePCC air electrodes, they have deficient protonic properties and even degrade under the steam-rich atmospheres characteristic of PCFC operation.[20–23]

Seeking a different approach, various studies have attempted to introduce electronic conductivity by doping rare earth metals and transition metals into $BaZrO_{3-\delta}$ (BZO)/$BaCeO_{3-\delta}$-based proton conductors to synthesize materials such as $BaCe_{0.5}Bi_{0.5}O_{3-\delta}$, cobalt-substituted $BaZr_{0.1}Ce_{0.7}Y_{0.2}O_{3-\delta}$ and BZO.[24–26] However, these materials are still poor $O^{2-}$ and $e^-$ conductors, resulting in limited performance. Recently, state-of-the-art cobalt-based air electrodes, such as $PrBa_{0.5}Sr_{0.5}Co_{1.5}Fe_{0.5}O_{5+\delta}$ (PBSCF) and $BaCo_{0.4}Fe_{0.4}Zr_{0.1}Y_{0.1}O_{3-\delta}$ (BCFZY), were used in high-performance intermediate-temperature RePCCs.[6,8] However, the thermal compatibility of these electrodes with other cell components remains a major concern due to the high thermal expansion coefficient (TEC) of cobalt-based perovskites (i.e., BCFZY: $21.6 \times 10^{-6}\ K^{-1}$ at 300–700 °C; PBSCF: $21.3 \times 10^{-6}\ K^{-1}$ at 250–900 °C).[27,28]

Meanwhile, an O-SOFC nanocomposite electrode was proposed to realize both high ORR activity and reduced TEC ($16.8 \times 10^{-6}\ K^{-1}$). This multiphase nanocomposite cathode for O-SOFC consisted of a primary phase of a tetragonal $SrFeO_{3-\delta}$ (SF)-based perovskite, $Sr_aCe_bFe_cNi_dO_{3-\delta}$ (T-SCFN), and three minor phases, including a Ruddlesden-Popper (RP)$Sr_4Fe_3O_{10-\delta}$ (RP-SF) based perovskite, $Sr_xCe_yFe_mNi_nO_{3-\delta}$ (RP-SCFN), and surface enriching nanoparticles of $CeO_2$ and NiO, by introducing a $Sr_{0.9}Ce_{0.1}Fe_{0.8}Ni_{0.2}O_{3-\delta}$ (SCFN) precursor. This electrode showed outstanding ORR activity when combined with an oxygen-conducting, samarium-doped ceria electrolyte.[29] Therefore, the multiphase nanocomposite air electrode can be introduced into to the RePCC system based on the idea that all three conductive ion ($H^+/O^{2-}/e^-$) properties could be excellent due to the different properties of the various materials making up the nanocomposite.

In this study, we demonstrate for the first time, that nanocomposites can be leveraged to develop superior RePCC air electrodes. Our developed SCFN-based nanocomposite showed outstanding ORR and OER activity. Both calculations and experiments suggest that the RP phase in SCFN promotes hydration and proton conduction, while the nanoscale NiO and $CeO_2$ phases foster $O_2$ surface exchange and $O^{2-}$ transfer from the RP or NiO phase surface to the primary phase. The RePCCs based on Ni-$BaZr_{0.1}Ce_{0.7}Y_{0.1}Yb_{0.1}O_{3-\delta}$ (BZCYYb) fuel electrode, BZCYYb electrolyte, and SCFN nanocomposite air electrode exhibited a high peak power density (PPD) of 531 mW cm$^{-2}$ in fuel cell mode and a current density of −364 mA cm$^{-2}$ at 1.3 V in electrolysis mode at 600 °C, while retaining robust operational stability of 120 h in fuel cell/electrolysis cycles at 550 °C. This investigation demonstrates that nanocomposites can be leveraged to realize highly active and durable air electrodes for RePCCs. The principle behind this work is that careful control of different nanoscale functional phases within the composite can create a bulk material with simultaneously optimized OER and ORR activities. Further, self-assembled nanocomposites experience strong interphase interaction, which inhibits

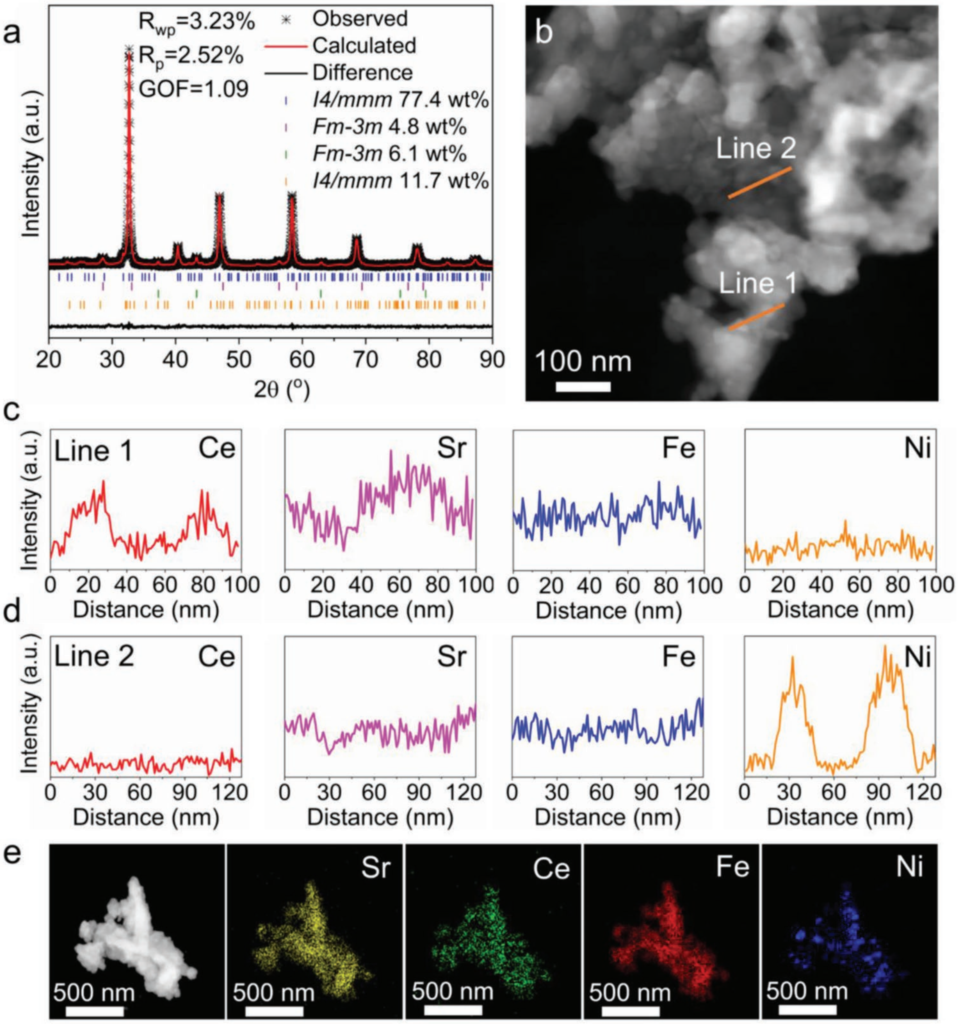

**Figure 2.** a) Refined X-ray diffraction (XRD) profiles of SCFN sample. b) Scanning transmission electron microscopy (STEM) image of SCFN sample and corresponding line energy dispersive X-ray (EDX) scan of c) $CeO_2$ and d) NiO nanoparticles, and e) STEM-mapping results of SCFN.

nanocatalyst agglomeration and reduces the total TEC of the material, thus ensuring the outstanding operational stability of the RePCCs.

## 2. Results and Discussion

The prepared nanocomposite was synthesized following a facile one-pot synthesis method.[30] Formation of the nanocomposite was confirmed by XRD characterization and corresponding Rietveld refinement, which suggested that the SCFN contained two major perovskite phases, i.e., SF-based and RP-SF-based perovskites (T-SCFN and RP-SCFN), and two minor oxide phases, i.e., NiO and $CeO_2$ phases (**Figure 2**a). For comparison, single-phase SF and dual-phase $Sr_{0.9}Fe_{0.8}O_{3-\delta}$ (SF98), which is composed of SF and RP-SF, were also prepared (Figure S1, Supporting Information). To identify morphology and composition, scanning electron microscopy (SEM), STEM, and EDX analysis were carried out. Unlike single-phase SF and dual phase SF98, the surface of SCFN was nanoparticle enriched (Figure S2, Supporting Information). The STEM image (Figure 2b) and corresponding line EDX results (Figure 2c,d) suggest that these nanoparticles were $CeO_2$ and NiO. STEM-Mapping results (Figure 2e) suggest that Ce and Ni were introduced into the major perovskite phases.[29] The valence states of the transition metals in SF, SF98, and SCFN were also analyzed (Figure S3, Supporting Information).

It is well known that the ORR of a fuel cell with a protonic electrolyte is more complicated compared to that with an oxygen-ion conducting electrolyte.[7,31] To determine the electrochemical performance of the SCFN composite electrode in PCFC mode, electrochemical impedance spectroscopy (EIS) was performed on BZCYYb-supported symmetric cells at varied air humidification (0, 3, 6 vol% $H_2O$) and temperature (450–650 °C) (Table S1, Supporting Information). It should be noted that no additional phases were identified by XRD analysis, implying that no reaction occurred between SCFN and BZCYYb (Figure S4, Supporting Information). The area specific resistance (ASR) and activation energy both decreased with increasing gas steam content, suggesting that hydration and

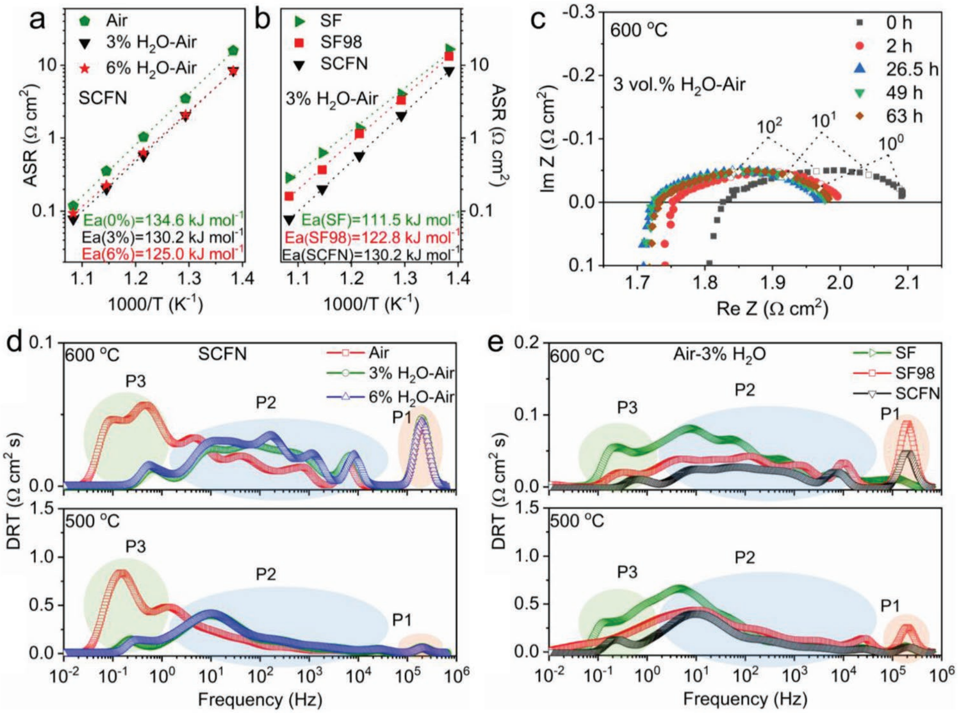

**Figure 3.** a) Arrhenius plots of the ASRs of the SCFN air electrode with BZCYYb electrolyte in 0, 3, 6 vol% $H_2O$-air at 450–650 °C. b) Arrhenius plots of the ASRs of the SF, SF98, and SCFN air electrodes with BZCYYb electrolytes in 3 vol% $H_2O$-air at 450–650 °C. c) Nyquist plots of SCFN composite electrode with BZCYYb electrolyte in 3 vol% $H_2O$-air at 600 °C for 63 h. Distribution of relaxation time (DRT) analysis of d) SCFN composite electrode under different steam content conditions at 500 °C and 600 °C, e) SF, SF98 composite, and SCFN composite electrodes under 3 vol% $H_2O$-Air at 500 °C and 600 °C.

proton conduction affect electrochemical activity (**Figure 3**a).[31] A symmetric cell based on a BZCYYb electrolyte with the SCFN composite cathode exhibited low ASR values of 0.078, 0.20, 0.57, 2.05, and 8.46 Ω $cm^2$ at 650, 600, 550, 500, and 450 °C, respectively, in 3 vol% $H_2O$-air (Figure 3a). The ASR values of the SCFN composite are lower than reported cobalt-free PCFC cathodes, demonstrating the exceptional performance of this nanocomposite electrode (Figure S5, Supporting Information).

To further assess the functionality of the SCFN electrode component phases, symmetric cells based on single-phase SF, and two-phase SF98 were also fabricated and tested (Figure S6a,b, Table S1, Supporting Information). As shown in Figure 3b, SF had the highest ASR values in wet air (3 vol% $H_2O$-Air). The SF98 composite electrode had lower ASR values than SF, suggesting that the RP-phase improved the ORR activity in PCFC mode (Figure 3b). Adding NiO and $CeO_2$ nanoparticles (to make SCFN) further decreased the ASR, implying that nano NiO and $CeO_2$ also enhanced ORR (Figure 3b). The ASR values of SF electrode are 0.63 and 4.02 Ω $cm^{-2}$ at 600 and 500 °C, respectively, while the corresponding values for the other two materials are significantly lower (0.37 and 3.31 Ω $cm^{-2}$ for SF98 and 0.20 and 2.05 Ω $cm^{-2}$ for SCFN) (Figure S7, Supporting Information). The SCFN composite also demonstrated decreased ohmic (Figure 3c) and stable polarization resistance (Figure S8, Supporting Information) during a 63 h test, implying good electrode/electrolyte contact and excellent operational stability.

To investigate the roles that RP-SF-based perovskite and surface-enriched nano NiO/$CeO_2$ play in promoting the ORR, the EIS data was analyzed with the DRT model. Using the DRT tools package,[32,33] the electrochemical processes were deconvolved into separate peaks,[34] as illustrated in Figure 3d,e, which could be divided into three regions denoted as P1, P2, and P3. It has been suggested that the high-frequency region (P1) represents the transfer of ions from the electrolyte to the cathode at the triple-phase boundary.[34] It is also understood that intermediate-frequency (P2) corresponds to the surface exchange and bulk diffusion and that low-frequency (P3) indicates gas diffusion (steam and $O_2$).[30,35,36] The area under a specific peak represents the resistance of the corresponding process. The P3 of SCFN drops sharply after steam is introduced (Figure 3d), implying decreased resistance (P3).[30,36] Conversely, the areas under P1 and P2 are relatively unchanged.

As reported in the literature, pure SF shows poor hydration capability (a proton uptake of 0.01–0.03% at 200–300 °C).[37] However, the RP-SF-based perovskites possess good proton uptake.[38] As a result, it is likely that the RP-SF phase simultaneously promotes hydration and proton transfer. To test this hypothesis, we compared the ASRs and DRTs of the SF and SF98 composites measured at 3 vol% $H_2O$-$N_2$, eliminating the influence of $O_2$ diffusion, oxygen-related surface exchange, and $O^{2-}$ transfer (Figure S9, Supporting Information). The SF98 composite had lower ASRs and activation energies than SF in the 550–650 °C range (Figure S9a, Supporting Information). From the DRT analysis, this enhancement can be attributed to $H_2O$ diffusion (P3), associated with hydration and proton transfer (P2) (Figure S9b,c,d, Supporting Information). The DRT of SF and SF98 composites in 3 vol% $H_2O$-Air (Figure 3e) were also compared. The significantly lower resistances of P3 and P2 for the SF98 composite in comparison to SF single-phase suggest that, consistent with literature,[35] the RP-SF phase promotes steam/$O_2$ diffusion as well as surface exchange and ion transfer. Surprisingly, we noted that the values of P2 and P3 for SCFN composite are lower than those of the SF98 composite. This difference can be attributed to the introduction of NiO and $CeO_2$ nanoparticles, which provide additional reaction sites and improve the kinetics of the oxygen reaction.[29] The EIS and DRT analysis suggests that the SCFN composite has fast surface exchange kinetics and $H^+/O^{2-}/e^-$ triple conductivity; both are critical properties to ORR/OER activity.

We carried out density functional theory (DFT) calculations to further understand the properties and roles of each perovskite phase in the SCFN nanocomposite. The XRD results shown suggest that SF and RP-SF can be modelled by $Sr_8Fe_8O_{23}$ (*I4/mmm*) and $Sr_4Fe_3O_{10}$ (*I4/mmm*), respectively (Figure S1, Supporting Information). The relaxed lattice parameters agree well with the XRD Rietveld refinement results. We calculated the oxygen vacancy formation energy ($\Delta E_{\text{vac}}$) as a proxy for the ORR/OER activity.[39] All distinct O sites in both materials were considered (Figure S10, Supporting Information). The calculated $\Delta E_{\text{vac}}$ values are listed (Table S2, Supporting Information); for $Sr_8Fe_8O_{23}$ and $Sr_4Fe_3O_{10}$, the lowest $\Delta E_{\text{vac}}$ are 1.12 and 1.09 eV, respectively. For $Sr_4Fe_3O_{10}$, the $\Delta E_{\text{vac}}$ in [SrO], i.e., the formation of one O1 vacancy, is 2.25 eV (Figure S10, Supporting Information), which is 1.19 eV greater than computed for [$SrFeO_3$], i.e., the $\Delta E_{\text{vac}}$ for one O3 vacancy. Therefore, the concentration of O vacancies might be higher in the [$SrFeO_3$] layers, likely leading to two-dimensional (2D) O-vacancy conduction.[40] In turn, the oxygen bulk diffusion is likely faster in RP-SF than that in SF, consistent with the literature.[29]

In addition to oxygen surface exchange and diffusion in protonic cells, hydration and proton transfer are also critical to ORR/OER. Consequently, the hydration energy ($\Delta E_{\text{hydr}}$) and proton migration barriers in SF and RP-SF were calculated. Regarding the hydration mechanism shown in (3) of Supporting Information, one $OH_O^{\bullet}$ fills in the oxygen vacant site that has the lowest $\Delta E_{\text{vac}}$, i.e., the O3 site in $Sr_4Fe_3O_{10}$ and the O1 site in $Sr_8Fe_8O_{23}$. We considered different configurations for the second $OH_O^{\bullet}$ and obtained the optimized hydrated SF and RP-SF structures with the lowest energies (Figure S11, Supporting Information). It can be observed that $OH_O^{\bullet}$ preferentially attaches to the O2 site of SF (Figure S11a, Supporting Information). For RP-SF, the two protons are located at the O3 sites (Figure S11b, Supporting Information). The $\Delta E_{\text{hydr}}$ for SF and RP-SF were predicted to be 0.67 and 0.44 eV, respectively, suggesting that hydration is more energetically favorable in RP-SF than SF.

To verify that the RP-SF phase promotes hydration, mass spectrometry (MS) and Fourier transform infrared spectroscopy (FTIR) characterizations were carried out. For MS and FTIR testing, the SF, SF98, and SCFN powder were first treated at 550 °C in 3 vol% $H_2O$-air (21 vol% $O_2$-79 vol% $N_2$) for 10 h. The steam was cut off when the temperature decreased to 100 °C to minimize the influence of the adsorbed water on the hydrated water signal. MS results showed that, in the 100–900 °C range, the $H_2O$ peak observed for SF is much weaker than the one for SF98 and SCFN, suggesting the stronger water adsorption and hydration capability of SF98 and SCFN compared to SF (**Figure 4**a). According to FTIR results, SF has a very weak $OH_O^{\bullet}$ peak between 3400 and 3800 $cm^{-1}$,[9] while the $OH_O^{\bullet}$ peak is more pronounced for the steam-treated SF98 and SCFN samples (Figure 4b). The MS and FTIR results are consistent with the calculated $\Delta E_{\text{hydr}}$ and further confirm that the presence of the RP-SF phase promotes hydration.

The proton migration barriers were also computed using the climbing image nudged elastic band (CI-NEB) method.[41] Two possible pathways for proton migration were considered, i.e., i) hopping from one octahedral vertex to a neighboring vertex, and ii) reorientation at the identical octahedral vertex (Figure S12, Supporting Information). Starting from the lowest energy configurations with one proton, which are labeled as site 1 in both Figure 4c,d, we considered different migration pathways for one $OH_O^{\bullet}$ in $Sr_{16}Fe_{16}O_{46}H$ and $Sr_{16}Fe_{12}O_{40}H$ to simulate the hydrated SF and RP-SF, respectively. The corresponding migration barriers are given in **Table 1**. The largest migration barriers for proton transport in $Sr_{16}Fe_{16}O_{46}H$ and $Sr_{16}Fe_{12}O_{40}H$ were predicted to be 0.48 and 0.34 eV, respectively. To estimate the $OH_O^{\bullet}$ transport in the *ab* plane, i.e., along the [100] and [010] directions in RP-SF, we also calculated the reorientation barrier of $OH_O^{\bullet}$ from 2 to 6 (Figure 4c). This barrier was predicted to be 0.24 eV, a value close to the one computed for the of $4 \rightarrow 5$ reorientation (0.26 eV) in the same material. The smaller migration barriers $OH_O^{\bullet}$ computed for RP-SF imply that the RP-SF phase is likely to promote proton migration.

The isotope exchange diffusion profiling (IEDP) method was used to identify proton diffusivity and surface exchange via time-of-flight secondary ion MS (ToF-SIMS).[42] Deuterium (D) was used as a tracer in the SCFN sample, allowing the estimation of SCFN's proton tracer diffusion coefficient ($D^*_{\text{H}}$) and surface exchange coefficient ($k^*_{\text{H}}$). The obtained $D^*_{\text{H}}$ and $k^*_{\text{H}}$ values of SCFN are shown (Figure S15a,b, Table S3, Supporting Information). The $D^*_{\text{H}}$ of SCFN increased with temperature due to thermal activation (Figure S15a, Supporting Information). In contrast, $k^*_{\text{H}}$ decreased with temperature because surface hydration is exothermic (Figure S15b, Supporting Information).[43] A noteworthy outcome of the experiment is that SCFN's $D^*_{\text{H}}$ is similar to the $D^*_{\text{H}}$ measured for proton-conducting electrolytes, such as $La_{27.15}W_{4.85}O_{55.28}V_{0.73}$ (LWO56),[44] $BaCe_{0.9}Y_{0.1}O_{3-\delta}$ (BCY10),[45] $(Ba_{0.965}Gd_{0.035})(Ce_{0.935}Gd_{0.035})O_{3-\delta}$ (Gd-BCO),[46] and $SrCe_{0.95}Yb_{0.05}O_{3-\delta}$ (SCY), indicating that SCFN is characterized by sufficient proton mobility and surface exchange properties (**Figure 5**a). The characterizations reported above suggest that, in addition to being a material with good $O^{2-}/e^-$ mixed conductivity and oxygen surface exchange kinetics, SCFN is an excellent $H^+$ conductor with a fast surface exchange.

To evaluate the performance of the SCFN composite in PCFCs, an anode supported single cell consisting of a NiO-BZCYYb fuel electrode, BZCYYb electrolyte (26.0 µm) and SCFN composite air electrode (9.6 µm) was manufactured (Figure S16, Supporting Information). The power output and EIS data were obtained by supplying pure $H_2$ and ambient air

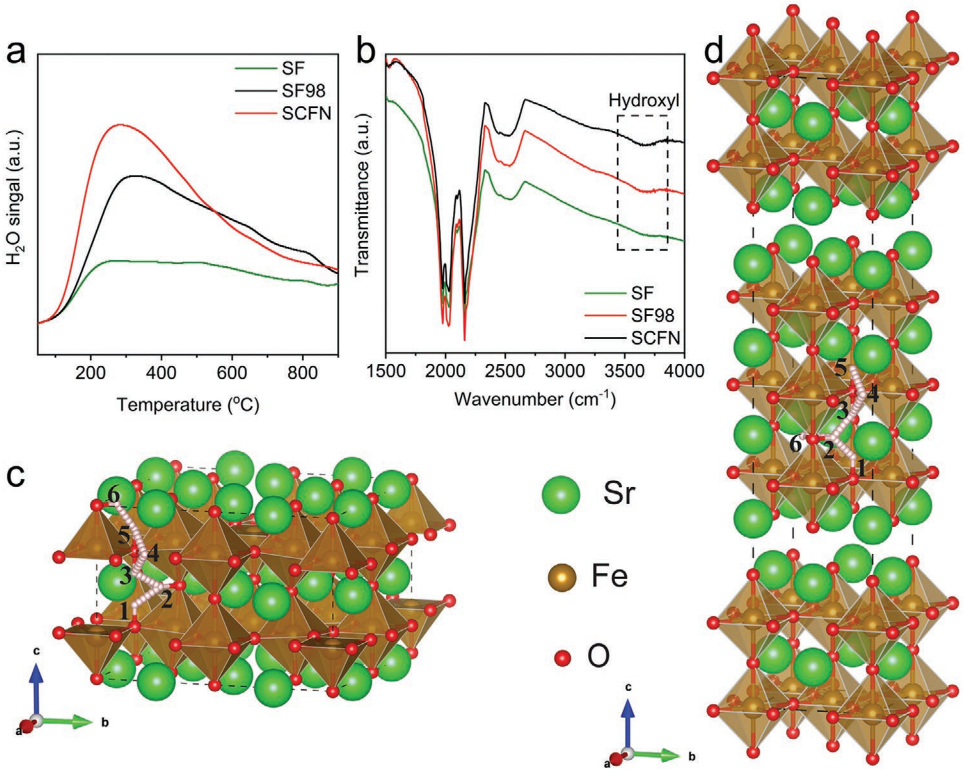

**Figure 4.** a) $H_2O$ temperature programmed desorption and b) FTIR profiles of steam-treated SF, SF98, and SCFN powders with the region for adsorbed water and proton defect. Distinct $OH_O^{\bullet}$ sites in c) $Sr_{16}Fe_{16}O_{46}H$ (hydrated SF) and d) $Sr_{16}Fe_{12}O_{40}H$ (hydrated RP-SF).

to the fuel and air electrodes. As seen in Figure 5b, the cell with the SCFN composite cathode exhibited PPDs of 745, 531, 347, and 225 mW cm$^{-2}$ at 650, 600, 550, and 500 °C, respectively. These excellent characteristics were also confirmed by the small polarizations measured by EIS (Figure S17, Supporting Information). The fuel cell's performance exceeds the performance of many reported cells with cobalt-free electrodes and even cobalt-based electrodes (Table S4, Supporting Information), and displayed excellent operational stability of over 290 h with no detectable degradation (Figure 5c). These results demonstrate the potential of the SCFN composite cathode in PCFCs.

We also used a similar cell for electrochemical reversibility tests. The *I–V* curves and EIS data were obtained by supplying pure $H_2$ and 3 vol% $H_2O$-air to the fuel and air electrodes, respectively (Figure 5d). The reversible cell in fuel cell mode had lower power output than the first cell due to the slight difference in cell preparation and the introduction of steam in the air electrode (Figure S18, Supporting Information). As seen in Figure 5c, the cell current densities were −364, −269, −179, and −91 mA cm$^{-2}$, at 600, 550, 500, and 450 °C, respectively, at 1.3 V. The performance in electrolysis mode exceeds many reported cells with cobalt-free and even cobalt-based electrodes (Table S5, Supporting Information). The excellent performance in electrolysis (1.3 V) and fuel cell (0.8 V) mode was also confirmed by the small polarization measured by EIS (Figure S19, Supporting Information). Cell reversibility was evaluated by cyclic operation between 1.3 V (electrolysis mode) and 0.8 V (fuel cell mode) at 550 °C. The current was measured for 10 h (first 2 cycles) and 4 h (last 25 cycles) at each condition in an alternating fashion (Figure 5e). Negligible performance degradation was detected throughout 27 reversible cycles (120 h). To assess the stability of the SCFN nanocomposite air electrode in conditions representative of practical RePCCs, the electrode was exposed to high steam concentration in electrolysis mode (Figure S20, Supporting Information). The cell operated stably for 44 h in 30 and 50 vol% $H_2O$-Air with no obvious degradation, suggesting that the SCFN nanocomposite has potential to operate at high steam concentrations. The Faradaic efficiency (FE) and $H_2$ production rate of the cell at 550 °C under an atmospheric composition of 30 and 50 vol% water vapor in air were also evaluated. The FE increased rapidly with increasing current and water vapor content, corroborating previous literature results.[6] The FE reached ≈89% (Figure 5f) at an electrolysis current density of −800 mA cm$^{-2}$ in 50 vol% $H_2O$-Air with a corresponding

**Table 1.** Migration barriers for one proton hopping or reorientating between the sites of $Sr_4Fe_3O_{10}$ and $Sr_8Fe_8O_{23}$ labeled in Figure 4c,d.

| | Proton migration barrier [eV] | | | | | |
|---|---|---|---|---|---|---|
| Migration path | 1 → 2 | 2 → 3 | 3 → 4 | 4 → 5 | 5 → 6 | 2 → 6 |
| $Sr_{16}Fe_{12}O_{40}H$ | 0.34 | 0.17 | 0.05 | 0.26 | | 0.24 |
| $Sr_{16}Fe_{16}O_{46}H$ | 0.26 | 0.22 | 0.34 | 0.17 | 0.48 | |
| Migration path | 6 → 5 | 5 → 4 | 4 → 3 | 3 → 2 | 2 → 1 | |
| $Sr_{16}Fe_{12}O_{40}H$ | | 0.05 | 0.26 | 0.03 | 0.33 | |
| $Sr_{16}Fe_{16}O_{46}H$ | 0.22 | 0.11 | 0.29 | 0.26 | 0.22 | |

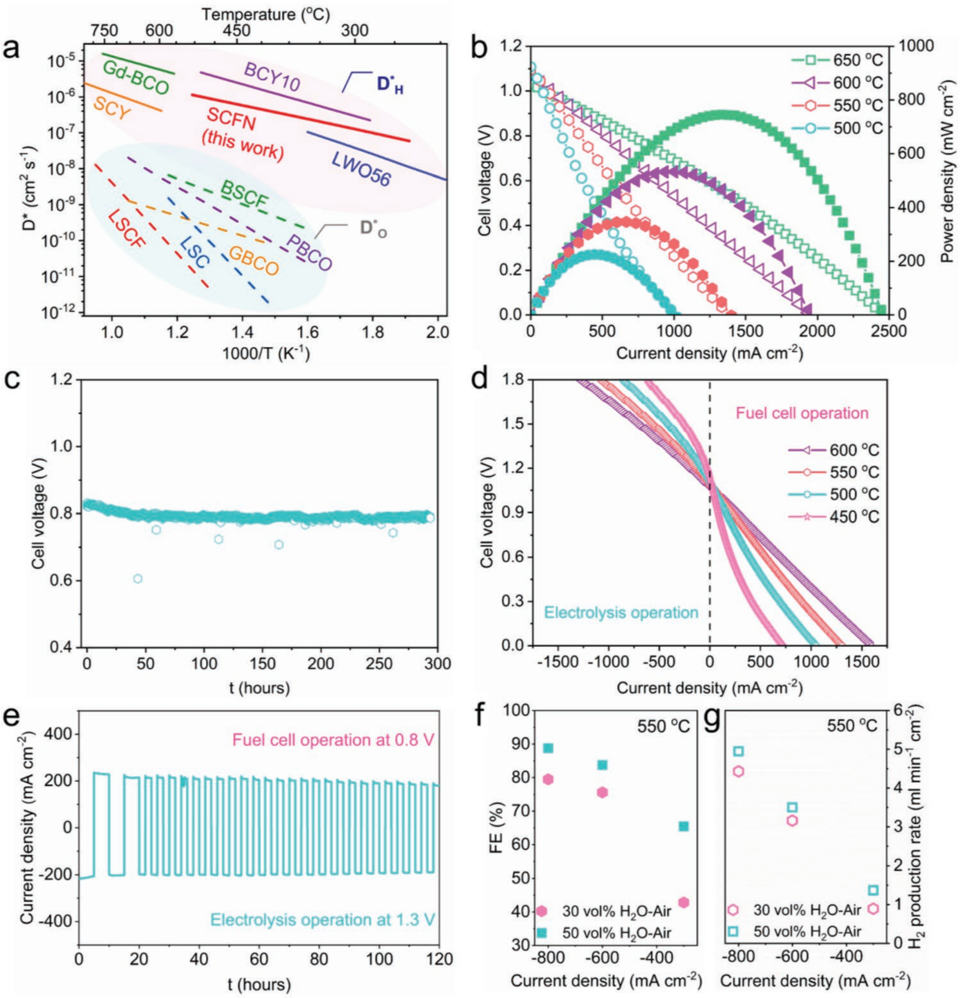

**Figure 5.** a) Comparison of $D^*_H$ of the SCFN with other representative MIEC materials and proton conductors: $Ba_{0.5}Sr_{0.5}Co_{0.8}Fe_{0.2}O_{3-\delta}$ (BSCF),[47] $PrBaCo_2O_{5+\delta}$ (PBCO),[48] $GdBaCo_2O_{5+\delta}$ (GBCO),[49] $La_{0.6}Sr_{0.4}Co_{0.2}Fe_{0.8}O_{3-\delta}$ (LSCF),[50] $La_{0.6}Sr_{0.4}CoO_{3-\delta}$ (LSC),[51] LWO56,[44] BCY10,[45] Gd-BCO,[46] and SCY.[52] Lines in the gray and blue circles represent $D^*$ values for oxygen ion and proton, respectively. b) $I$–$V$ and $I$–$P$ curves of the Ni-BZCYYb anode supported cell in $H_2$ fuel at 500–650 °C. c) Operational stability of the Ni-BZCYYb anode supported cell in $H_2$ fuel at 550 °C. d) $I$–$V$ curves of the Ni-BZCYYb anode supported cell measured in electrolysis mode in $H_2$ fuel at 450–600 °C. e) Continuous RePCC operation, cycling between electrolysis and fuel cell mode at 550 °C. The oscillation in the stability curve observed at ≈35 h was due to an air supply malfunction. f) Faradaic efficiency (FE) and g) $H_2$ production rate of RePCC with SCFN as air electrode, measured at different current densities under 30 and 50 vol% $H_2O$-Air at 550 °C.

$H_2$ production rate of 4.95 mL min$^{-1}$ cm$^{-2}$ (Figure 5g), further suggesting great potential of the SCFN nanocomposite for water splitting in RePCCs.

The developed SCFN nanocomposite electrode illustrates the key advantages of nanocomposite electrodes as follows: 1) each phase of the nanocomposite has a different function, synergistically meeting the demanding requirements of the RePCC air electrode; 2) nanoscale contact between the multiple phases leads to a large concentration of OER and ORR catalytic centers, ensuring excellent bifunctional activity; and 3) in a self-assembled nanocomposite, the strong interphase interaction inhibits sintering of the nanocatalyst during operation, ensuring electrode longevity. The strong interphase interaction may also limit thermal expansion, improving thermal compatibility between air electrode and electrolyte. The combination of these factors contributes to a highly active and stable RePCC air electrode.

## 3. Conclusion

In conclusion, this work demonstrates the potential of nanocomposites as a new avenue for the development of high-performance RePCC air electrodes through the development of a multiphase SCFN nanocomposite electrode. This electrode showed both high ORR and OER activity and excellent operational stability. Ni-BZCYYb anode-supported RePCCs with an SCFN air electrode achieved a high PPD of 531 mW cm$^{-2}$ and electrolysis current of −364 mA cm$^{-2}$, while maintaining excellent reversible stability for 120 h at 550 °C with negligible degradation. The SCFN electrode constituted four phases; SF-based single-phase perovskite, RP-SF-based perovskite, and a $CeO_2$ and NiO nanoparticle enriched surface. Experiments suggest that the RP phase promoted gas (steam/$O_2$) diffusion and the related steam/$O_2$ surface exchange reaction, thus enhancing electrochemical activity. The NiO and $CeO_2$ nanoparticles further promoted the $O_2$ adsorption/dissociation and $O^{2-}$ transfer from the surface to the major phase. DFT calculations suggest the role of the RP phase in promoting hydration, and proton and $O^{2-}$ transfer, implying that SCFN composite has fast steam/$O_2$ surface exchange kinetics and good $H^+$/$O^{2-}$/$e^-$ triple conducting capability, contributing to high ORR/OER activity. The SCFN composite performance exceeds most reported cobalt-free air electrodes and is comparable to state-of-the-art cobalt-based perovskite electrodes in the literature. This study emphasizes that the RP phase promotes both the ORR and OER of RePCCs and provides a promising direction for the future development of high-performance air electrodes.

## Supporting Information

Supporting Information is available from the Wiley Online Library or from the author.

## Acknowledgements

Y.S., J.L., and Y.W. contributed equally to this work. The authors gratefully acknowledge the support of the Research Grant Council of Hong Kong (General Research Fund 16201820 and 16206019), the Nano & Material Technology Development Project (NRF-2021M3H4A1A01002919), and the Grobal Ph.D Fellowship (2018H1A2A1060644) through the National Research Foundation (NRF) of Korea, funded by the Ministry of Science, ICT, and Future Planning. M.J.R. thanks the Hong Kong PhD Fellowship Scheme for financial support.

## Conflict of Interest

The authors declare no conflict of interest.

## Data Availability Statement

Research data are not shared.

## Keywords

air electrodes, bifunctional, nanocomposites, perovskites, reversible protonic ceramic cells

Received: June 20, 2021
Revised: July 21, 2021

[1] Y. Wang, T. Liu, L. Lei, F. Chen, *Fuel Process. Technol.* **2017**, *161*, 248.
[2] Y. Zhou, E. Liu, Y. Chen, Y. Liu, L. Zhang, W. Zhang, Z. Luo, N. Kane, B. Zhao, L. Soule, Y. Niu, Y. Ding, H. Ding, D. Ding, M. Liu, *ACS Energy Lett.* **2021**, *6*, 1511.
[3] Y. Song, W. Wang, L. Ge, X. Xu, Z. Zhang, P. S. B. Julião, W. Zhou, Z. Shao, *Adv. Sci.* **2017**, *4*, 1700337.
[4] R. Murphy, Y. Zhou, L. Zhang, L. Soule, W. Zhang, Y. Chen, M. Liu, *Adv. Funct. Mater.* **2020**, *30*, 2002265.
[5] G. Yang, C. Su, H. Shi, Y. Zhu, Y. Song, W. Zhou, Z. Shao, *Energy Fuels* **2020**, *34*, 15169.
[6] C. Duan, R. Kee, H. Zhu, N. Sullivan, L. Zhu, L. Bian, D. Jennings, R. O'Hayre, *Nat. Energy* **2019**, *4*, 230.
[7] C. Duan, J. Huang, N. Sullivan, R. O'Hayre, *Appl. Phys. Rev.* **2020**, *7*, 011314.
[8] S. Choi, T. C. Davenport, S. M. Haile, *Energy Environ. Sci.* **2019**, *12*, 206.
[9] H. Ding, W. Wu, C. Jiang, Y. Ding, W. Bian, B. Hu, P. Singh, C. J. Orme, L. Wang, Y. Zhang, *Nat. Commun.* **2020**, *11*, 1907.
[10] Y. Zheng, J. Wang, B. Yu, W. Zhang, J. Chen, J. Qiao, J. Zhang, *Chem. Soc. Rev.* **2017**, *46*, 1427.
[11] M. Papac, V. Stevanović, A. Zakutayev, R. O'Hayre, *Nat. Mater.* **2021**, *20*, 301.
[12] B. Hu, A. N. Aphale, M. Reisert, S. Belko, O. A. Marina, J. W. Stevenson, P. Singh, *ECS Trans.* **2018**, *85*, 13.
[13] L. Lei, Z. Tao, X. Wang, J. P. Lemmon, F. Chen, *J. Mater. Chem. A* **2017**, *5*, 22945.
[14] J. Kim, A. Jun, O. Gwon, S. Yoo, M. Liu, J. Shin, T.-H. Lim, G. Kim, *Nano Energy* **2018**, *44*, 121.
[15] S. D. Graves, S. H. Ebbesen, S. B. Jensen, *Nat. Mater.* **2015**, *14*, 239.
[16] Y. Meng, J. Gao, H. Huang, M. Zou, J. Duffy, J. Tong, K. S. Brinkman, *J. Power Sources* **2019**, *439*, 227093.
[17] Y. Song, H. Li, M. Xu, G. Yang, W. Wang, R. Ran, W. Zhou, Z. Shao, *Small* **2020**, *16*, 2001859.
[18] W. Tang, H. Ding, W. Bian, W. Wu, W. Li, X. Liu, J. Y. Gomez, C. Y. R. Vera, M. Zhou, D. Ding, *J. Mater. Chem. A* **2020**, *8*, 14600.
[19] M. A. Azimova, S. McIntosh, *Solid State Ionics* **2011**, *203*, 57.
[20] A. Grimaud, F. Mauvy, J. M. Bassat, S. Fourcade, L. Rocheron, M. Marrony, J. C. Grenier, *J. Electrochem. Soc.* **2012**, *159*, B683.
[21] S. Li, K. Xie, *J. Electrochem. Soc.* **2013**, *160*, F224.
[22] S. Sun, Z. Cheng, *J. Electrochem. Soc.* **2017**, *164*, F3104.
[23] H. An, H.-W. Lee, B.-K. Kim, J.-W. Son, K. J. Yoon, H. Kim, D. Shin, H.-I. Ji, J.-H. Lee, *Nat. Energy* **2018**, *3*, 870.
[24] Z. Tao, L. Bi, L. Yan, W. Sun, Z. Zhu, R. Peng, W. Liu, *Electrochem. Commun.* **2009**, *11*, 688.
[25] L. Yang, S. Wang, X. Lou, M. Liu, *Int. J. Hydrogen Energy* **2011**, *36*, 2266.
[26] Y. Rao, S. Zhong, F. He, Z. Wang, R. Peng, Y. Lu, *Int. J. Hydrogen Energy* **2012**, *37*, 12522.
[27] C. Duan, D. Hook, Y. Chen, J. Tong, R. O'Hayre, *Energy Environ. Sci.* **2017**, *10*, 176.
[28] L. Jiang, T. Wei, R. Zeng, W.-X. Zhang, Y.-H. Huang, *J. Power Sources* **2013**, *232*, 279.
[29] Y. Song, Y. Chen, M. Xu, W. Wang, Y. Zhang, G. Yang, R. Ran, W. Zhou, Z. Shao, *Adv. Mater.* **2020**, *32*, 1906979.
[30] R. Ren, Z. Wang, C. Xu, W. Sun, J. Qiao, D. W. Rooney, K. Sun, *J. Mater. Chem. A* **2019**, *7*, 18365.
[31] Y. Song, Y. Chen, W. Wang, C. Zhou, Y. Zhong, G. Yang, W. Zhou, M. Liu, Z. Shao, *Joule* **2019**, *3*, 2842.
[32] T. H. Wan, M. Saccoccio, C. Chen, F. Ciucci, *Electrochim. Acta* **2015**, *184*, 483.
[33] M. Saccoccio, T. H. Wan, C. Chen, F. Ciucci, *Electrochim. Acta* **2014**, *147*, 470.
[34] Y. Chen, Y. Choi, S. Yoo, Y. Ding, R. Yan, K. Pei, C. Qu, L. Zhang, I. Chang, B. Zhao, *Joule* **2018**, *2*, 938.
[35] F. He, M. Liang, W. Wang, R. Ran, G. Yang, W. Zhou, Z. Shao, *Energy Fuels* **2020**, *34*, 11464.
[36] Y. Bu, S. Joo, Y. Zhang, Y. Wang, D. Meng, X. Ge, G. Kim, *J. Power Sources* **2020**, *451*, 227812.
[37] R. Zohourian, R. Merkle, G. Raimondi, J. Maier, *Adv. Funct. Mater.* **2018**, *28*, 1801241.
[38] D. Pelloquin, J. Hadermann, M. Giot, V. Caignaert, C. Michel, M. Hervieu, B. Raveau, *Chem. Mater.* **2004**, *16*, 1715.

[39] J. Liu, J. Wang, A. Belotti, F. Ciucci, *ACS Appl. Energy Mater.* **2019**, *2*, 5472.
[40] X. Xu, Y. Pan, Y. Zhong, R. Ran, Z. Shao, *Mater. Horiz.* **2020**, *7*, 2519.
[41] G. Henkelman, B. P. Uberuaga, H. Jónsson, *J. Chem. Phys.* **2000**, *113*, 9901.
[42] A. Seong, J. Kim, D. Jeong, S. Sengodan, M. Liu, S. Choi, G. Kim, *Adv. Sci.* **2021**, *8*, 2004099.
[43] T. Norby, *Solid State Ionics* **1999**, *125*, 1.
[44] R. Hancke, S. Fearn, J. A. Kilner, R. Haugsrud, *Phys. Chem. Chem. Phys.* **2012**, *14*, 13971.
[45] K. D. Kreuer, W. Münch, U. Traub, J. Maier, *Ber. Bunsenges. Phys. Chem.* **1998**, *102*, 552.
[46] K. D. Kreuer, E. Schönherr, J. Maier, *Solid State Ionics* **1994**, *70*, 278.
[47] V. B. Vert, J. M. Serra, J. A. Kilner, M. Burriel, *J. Power Sources* **2012**, *213*, 270.
[48] M. Burriel, *Chem. Mater.* **2012**, *24*, 613.
[49] A. Tarancón, S. J. Skinner, R. J. Chater, F. Hernandez-Ramirez, J. A. Kilner, *J. Mater. Chem.* **2007**, *17*, 3175.
[50] A. Leonide, B. Rüger, A. Weber, W. A. Meulenberg, E. Ivers-Tiffée, *J. Electrochem. Soc.* **2009**, *157*, B234.
[51] A. V. Berenov, A. Atkinson, J. A. Kilner, E. Bucher, W. Sitte, *Solid State Ionics* **2010**, *181*, 819.
[52] H. Uchida, H. Yoshikawa, T. Esaka, S. Ohtsu, H. Iwahara, *Solid State Ionics* **1989**, *36*, 89.